Frequency Scanning-Based Contributions Identification of Current Control Loop and PLL on DQ Impedance Characteristics of Three-Phase Grid-Connected Inverter

Zhou, Weihua; Wang, Yanbo; E. Torres-Olguin, Raymundo; Chen, Zhe

Published in:
The 12th Annual IEEE Energy Conversion Congress and Exposition (ECCE 2020)

Publication date:
2020

Document Version
Accepted author manuscript, peer reviewed version

Citation for published version (APA):
Zhou, W., Wang, Y., E. Torres-Olguin, R., & Chen, Z. (Accepted/In press). Frequency Scanning-Based Contributions Identification of Current Control Loop and PLL on DQ Impedance Characteristics of Three-Phase Grid-Connected Inverter. In *The 12th Annual IEEE Energy Conversion Congress and Exposition (ECCE 2020)*

Frequency Scanning-Based Contributions Identification of Current Control Loop and PLL on DQ Impedance Characteristics of Three-Phase Grid-Connected Inverter

Weihua Zhou*, Yanbo Wang*, Raymundo E. Torres-Olguin† and Zhe Chen*
*Department of Energy Technology, Aalborg University, Aalborg, Denmark
wez@et.aau.dk, ywa@et.aau.dk, zch@et.aau.dk
†SINTEF Energy Research Institute, Trondheim, Norway
raymundo.torres-olguin@sintef.no

***Abstract*—Complex space vector and complex transfer function theory is used to theoretically establish the dq impedance model of current-controlled grid-connected inverter (GCI) with considering phase-locked loop (PLL) dynamics, where contributions of current control loop and PLL on dq impedance characteristics are clearly identified. On its basis, this paper presents a frequency scanning-based black box identification method of the contributions of current control loop and PLL on dq-domain impedance characteristics of the GCI. Three-phase small-signal voltage vector perturbation which is aligned with point of common coupling (PCC) voltage vector is injected into PCC in series way, so that grid current responses which are only determined by the dynamics of current control loop are excited. In addition, parallel current injection to excite PCC voltage responses is theoretically proved to be not applicable for extracting the dynamics of current control loop and PLL. The effectiveness of the presented dq-domain impedance characteristics division method is verified by both frequency scanning results and time-domain simulation results obtained in Matlab/Simulink environment.**

***Index Terms*—Current control loop, dq-domain impedance, frequency scanning, grid-connected inverter, impedance characteristics division, phase-locked loop.**

I. INTRODUCTION

Voltage source grid-connected inverters (GCIs) have widely been utilized as the interface between the renewable energies, e.g., wind power and solar power, and utility grid [1]. However, the interactions between the control loops of the GCIs, e.g., current control loop and phase-locked loop (PLL), and time-varying grid impedance may lead to instability phenomena in wide frequency ranges [2]–[4]. Specifically, low-frequency instability phenomena can be induced under weak grid conditions, if PLL controller parameters are not properly tuned [5]. Recently, the impedance-based stability criteria (IBSC) has been proposed to assess the stability issues of three-phase AC power systems [6]. On its basis, the dq-domain IBSC is developed to deal with the impedance coupling effects which are caused by PLL and outer power control loop [7], [8].

The dq-domain impedance characteristic of the GCI is required for the dq-domain IBSC, which can be theoretically derived if the internal circuit and controller parameters are known in advance [7]. However, the information is sometimes confidential, due to the industry secrecy and intellectual property protection [9], [10]. Recently, the frequency scanning techniques have been developed to deal with the black issue [11]–[23]. The dq-domain impedance model is obtained in [11] by injecting an unbalanced line-to-line current between two lines of the AC power system. In [12], an algorithm is constructed to allow for the measurement of the dq-domain impedance model via injection on multiple axes which are synchronized to the three phase network via a variable bandwidth PLL. Based on the identification of transfer function models from the response of the GCI under a set of passive load step tests, a dq-domain impedance model identification algorithm is proposed in [13]. In addition, the dq-domain impedance model is measured in [14], [15] by injecting three-phase small voltage perturbation in series way or injecting three-phase small current perturbation in parallel way, whereas the dq-domain impedance model of the three-phase AC system is measured in [16], [17] by injecting single-phase small voltage perturbation. In [18], a single-phase perturbation is injected into the inverter system during two scanning cycles, based on which the self-impedance and accompanying-impedance which are employed to characterize the frequency coupling effect of the GCI can be obtained in the sequence-domain. In [19], another three-phase inverter is paralleled with the GCI under test to generate the injected voltage or current signals. In addition, an adaptive frequency injection method is proposed in [20], where smaller frequency interval of injection signals is used in the region containing peaks and valleys and larger frequency interval is used in the region approximating to straight line. Therefore, the accuracy, reliability and efficiency of the traditional frequency scanning methods can

---

This work was supported by the ForskEL and EUDP project "Voltage Control and Protection for a Grid towards 100% Power Electronics and Cable Network (COPE)" (Project No.: 880063).

be improved. However, these frequency scanning-based dq-domain impedance measurement methods presented in [11]–[20] require advanced and dedicated equipments, and have limited real-time applicability.

In [21], [22], orthogonal binary sequences which have wide bandwidths in nature are injected into the control loop of the GCI to simultaneously measure the d-axis and q-axis impedance components of the dq-domain impedance models of the GCI and the grid. In [23], the orthogonal binary sequences are further injected into a multiple-converter-based power system. Applying this method, all the impedances in the system can be simultaneously measured during one measurement cycle, so that the overall measurement time can be significantly reduced. However, these existing works can only reveal the overall effects of all control loops on the dq-domain impedance models. To the best of the authors' knowledge, no works have been reported on how to identify the contributions of different control loops on dq-domain impedance characteristics based on impedance measurement.

Complex space vectors and complex transfer functions-based modeling method of the GCI is originally proposed in [24], and has been extended to dq impedance modeling in [25], [26]. Specifically, current-controlled GCI and power-controlled GCI are investigated in [25] and [26], respectively. Complex space vectors and complex transfer function theory facilitates the observation of the effects of different control loops on dq-domain impedance feature. Based on the findings, this paper improves the conventional dq-domain impedance measurement techniques, and presents a frequency scanning-based black box identification method of contributions of current control loop and PLL on dq-domain impedance characteristics. The method presented in this paper is able to split the measured dq-domain impedance feature into two parts which are dominated by current control loop and PLL, respectively. In this case, the contributions of different control loops on system stability can be quantitatively assessed even if no detailed circuit and controller parameters are known.

II. EFFECTS OF CURRENT CONTROL LOOP AND PLL ON DQ-DOMAIN IMPEDANCE MODEL

In this section, the system configuration of the studied power system is first depicted. On its basis, the dq impedance models of a current-controlled three-phase LCL-filtered GCI without and with consideration of PLL are modeled using complex space vectors and complex transfer functions, respectively.

A. System Description

Fig. 1 shows the circuit and control diagram of a three-phase LCL-filtered voltage source GCI with current control loop and PLL. The LCL filter (L_{f1}, C_f and L_{f2}) is used to attenuate the high-frequency switching harmonics. The phase angle θ_g of voltage at point of common coupling (PCC) V_{PCC} is detected and synchronized with phase angle of injected current i_g of the GCI by the synchronous reference frame (SRF)-PLL, of which the detailed structure is shown in the red dotted box of Fig. 1. In addition, the grid-side current i_g is controlled in dq reference frame using proportional-integral (PI) controller. The grid impedance is emulated as an inductor L_g with parasitic resistor R_g which is paralleled with a capacitor C_g.

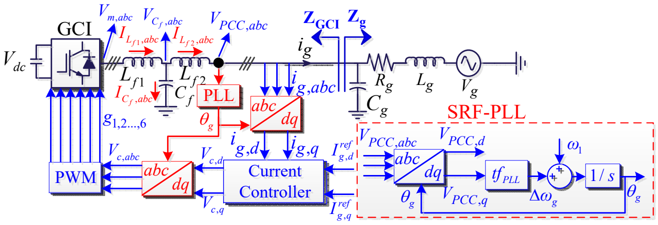

Fig. 1. Simplified one-line diagram of a three-phase LCL-filtered voltage source GCI with current control loop and PLL.

The dq impedance model of the GCI with consideration of current control loop and PLL has been established in [7], [25] using two-dimensional transfer matrices. In this paper, the dq impedance model will be established using complex space vectors and complex transfer functions. The italic letters are used to denote the real space vectors, e.g., $x_{dq} = [x_d, x_q]^T$ and $x_{\alpha\beta} = [x_\alpha, x_\beta]^T$. In addition, the bold letters are used to denote the complex space vectors, e.g., $\mathbf{x_{dq}} = x_d + jx_q$ and $\mathbf{x}_{\alpha\beta} = x_\alpha + jx_\beta$ for electrical parameters in dq-domain and $\alpha\beta$-domain, respectively, and complex transfer functions, e.g., $\mathbf{Y_{dq}} = Y_d + jY_q$ and $\mathbf{Y}_{\alpha\beta} = Y_\alpha + jY_\beta$ for admittance of the GCI in dq-domain and $\alpha\beta$-domain, respectively.

A linear continuous-time system with input signal and output signal as real space vectors $u_{dq} = [u_d, u_q]^T$ and $y_{dq} = [y_d, y_q]^T$ can be described as follows [24].

$$y_{dq} = \begin{bmatrix} G_{dd}(s) & G_{dq}(s) \\ G_{qd}(s) & G_{qq}(s) \end{bmatrix} u_{dq} = G^m(s)u_{dq} \tag{1}$$

where $G^m(s)$ is the transfer matrix between u_{dq} and y_{dq}. The superscript m indicates that the symbol is a matrix. For a symmetric three-phase AC system, i.e., $G_{dd}(s) = G_{qq}(s) = G_d(s)$ and $G_{qd}(s) = -G_{dq}(s) = G_q(s)$, (1) can be reformulated as (2) by representing $G(s)$ in the form of complex transfer function.

$$\mathbf{y_{dq}} = y_d + jy_q = \mathbf{G(s)u_{dq}} = [G_d(s) + jG_q(s)](u_d + ju_q) \tag{2}$$

On the other hand, only one complex transfer function $\mathbf{G(s)}$ is not sufficient for modeling an unsymmetric system. Instead, two complex transfer functions should be involved, shown as follows [24].

$$\mathbf{y_{dq}} = \mathbf{G_+(s)u_{dq}} + \mathbf{G_-(s)u^*_{dq}} \tag{3}$$

where superscript $*$ denotes conjugation, and

$$\begin{aligned} \mathbf{G_+(s)} &= \frac{\mathbf{G_{dd}(s)+G_{qq}(s)}}{\mathbf{2}} + \mathbf{j}\frac{\mathbf{G_{dq}(s)+G_{qd}(s)}}{\mathbf{2}} \\ \mathbf{G_-(s)} &= \frac{\mathbf{G_{dd}(s)-G_{qq}(s)}}{\mathbf{2}} + \mathbf{j}\frac{\mathbf{G_{dq}(s)-G_{qd}(s)}}{\mathbf{2}} \end{aligned} \tag{4}$$

Based on (3) and (4), the following equation holds.

$$\begin{bmatrix} \mathbf{y_{dq}} \\ \mathbf{y^*_{dq}} \end{bmatrix} = \begin{bmatrix} \mathbf{G_+(s)} & \mathbf{G_-(s)} \\ \mathbf{G^*_-(s)} & \mathbf{G^*_+(s)} \end{bmatrix} \begin{bmatrix} \mathbf{u_{dq}} \\ \mathbf{u^*_{dq}} \end{bmatrix} \tag{5}$$

B. Effect of Current Control Loop on DQ Impedance Model

According to (1) and (2), the inductor and capacitor can be represented as complex space vectors based on their dq impedance models, shown as follows.

$$\begin{aligned}
Z_{dq}^m(L) &= \begin{bmatrix} sL & -\omega_1 L \\ \omega_1 L & sL \end{bmatrix} \Leftrightarrow \mathbf{Z_{dq}(L)} = (s+j\omega_1)L \\
Y_{dq}^m(L) &= \tfrac{1}{L(s^2+\omega_1^2)} \begin{bmatrix} s & \omega_1 \\ -\omega_1 & s \end{bmatrix} \Leftrightarrow \mathbf{Y_{dq}(L)} = \tfrac{1}{(s+j\omega_1)L} \\
Z_{dq}^m(C) &= \tfrac{1}{C(s^2+\omega_1^2)} \begin{bmatrix} s & \omega_1 \\ -\omega_1 & s \end{bmatrix} \Leftrightarrow \mathbf{Z_{dq}(C)} = \tfrac{1}{(s+j\omega_1)C} \\
Y_{dq}^m(C) &= \begin{bmatrix} sC & -\omega_1 C \\ \omega_1 C & sC \end{bmatrix} \Leftrightarrow \mathbf{Y_{dq}(C)} = (s+j\omega_1)C
\end{aligned} \tag{6}$$

where ω_1 is the fundamental angular frequency of the grid voltage V_g. The dynamic equations of the LCL filter can be expressed as follows.

$$\begin{aligned}
&\mathbf{V_{m,dq}} - \mathbf{V_{C_f,dq}} = \mathbf{Z_{dq}(L_{f1})I_{L_{f1},dq}} \\
&\mathbf{V_{C_f,dq}} = \mathbf{Z_{dq}(C_f)I_{C_f,dq}} \\
&\mathbf{V_{C_f,dq}} - \mathbf{V_{PCC,dq}} = \mathbf{Z_{dq}(L_{f2})I_{L_{f2},dq}}
\end{aligned} \tag{7}$$

where $\mathbf{V_{m,dq}} = V_{m,d} + jV_{m,q}$, $\mathbf{V_{C_f,dq}} = V_{C_f,d} + jV_{C_f,q}$ and $\mathbf{V_{PCC,dq}} = V_{PCC,d} + jV_{PCC,q}$ are complex space vector representations of $V_{m,abc}$, $V_{C_f,abc}$ and $V_{PCC,abc}$ in Fig. 1, respectively. $\mathbf{Z_{dq}(L_{f1})}$, $\mathbf{Z_{dq}(L_{f2})}$ and $\mathbf{Z_{dq}(C_f)}$ are complex space vector representations of dq impedance models of L_{f1}, L_{f2} and C_f, respectively, which can be obtained by (6). In addition, $\mathbf{I_{L_{f1},dq}} = I_{L_{f1},d} + jI_{L_{f1},q}$, $\mathbf{I_{C_f,dq}} = I_{C_f,d} + jI_{C_f,q}$ and $\mathbf{I_{L_{f2},dq}} = \mathbf{I_{g,dq}} = I_{L_{f2},d} + jI_{L_{f2},q}$ are the complex space vector representations of $I_{L_{f1},abc}$, $I_{C_f,abc}$ and $I_{L_{f2},abc}$ in Fig. 1, respectively.

According to (7), $\mathbf{Y_{LCLl}}$ and $\mathbf{Y_{LCLr}}$ are defined as follows.

$$\begin{aligned}
\mathbf{Y_{LCLl}} &= \left.\frac{\mathbf{I_{g,dq}}}{\mathbf{V_{m,dq}}}\right|_{\mathbf{V_{PCC,dq=0}}} \\
&= \frac{\mathbf{Z_{dq}(C_f)}}{[\mathbf{Z_{dq}(C_f)}//\mathbf{Z_{dq}(L_{f2})}+\mathbf{Z_{dq}(L_{f1})}](\mathbf{Z_{dq}(C_f)}+\mathbf{Z_{dq}(L_{f2})})} \\
\mathbf{Y_{LCLr}} &= \left.\frac{\mathbf{I_{g,dq}}}{\mathbf{V_{PCC,dq}}}\right|_{\mathbf{V_{m,dq=0}}} = \frac{1}{\mathbf{Z_{dq}(C_f)}//\mathbf{Z_{dq}(L_{f1})}+\mathbf{Z_{dq}(L_{f2})}}
\end{aligned} \tag{8}$$

The control block diagram of the one-line diagram of the GCI in Fig. 1 without considering PLL dynamics can be established as Fig. 2, where the PLL-related control blocks are marked as red. The complex space vector representation of the terminal voltage of the GCI $\mathbf{V_{m,dq}}$ can be calculated based on the current control loop, shown as follows.

$$\mathbf{V_{m,dq}} = (\mathbf{I_{g,dq}^{ref}} - \mathbf{I_{g,dq}})\mathbf{G_{c,dq}G_{del}} \tag{9}$$

where $\mathbf{I_{g,dq}^{ref}} = I_{g,d}^{ref} + jI_{g,q}^{ref}$ and $\mathbf{I_{g,dq}} = I_{g,d} + jI_{g,q}$ are complex space vector representations of current references and actual grid current in dq-domain, respectively. In addition, $\mathbf{G_{c,dq}} = K_{cp} + K_{ci}/s$ and $\mathbf{G_{del}} = e^{-1.5sT_s}$ are the complex space vector representations of current controller and time delay which consists of one sampling period for computation and a half sampling period for PWM modulation [7]. $\mathbf{G_{c,dq}}$ and $\mathbf{G_{del}}$ can be calculated from the corresponding dq-domain models in (10) based on (1) and (2).

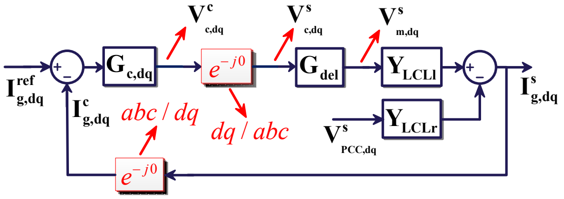

Fig. 2. Control block diagram of three-phase GCI in Fig. 1 using complex space vectors and complex transfer functions without considering PLL dynamics.

$$\begin{aligned}
G_{c,dq}^m &= \begin{bmatrix} G_{c,dq} & 0 \\ 0 & G_{c,dq} \end{bmatrix} = \begin{bmatrix} K_{cp} + \frac{K_{ci}}{s} & 0 \\ 0 & K_{cp} + \frac{K_{ci}}{s} \end{bmatrix} \\
G_{del}^m &= \begin{bmatrix} G_{del} & 0 \\ 0 & G_{del} \end{bmatrix} = \begin{bmatrix} e^{-1.5sT_s} & 0 \\ 0 & e^{-1.5sT_s} \end{bmatrix}
\end{aligned} \tag{10}$$

By combining (7) and (9), the closed-loop system response $\mathbf{I_{g,dq}}$ can be derived as follows.

$$\mathbf{I_{g,dq}} = \mathbf{G_{cl,dq}I_{g,dq}^{ref}} + \mathbf{Y_{cl,dq}V_{PCC,dq}} \tag{11}$$

where $\mathbf{G_{cl,dq}}$ and $\mathbf{Y_{cl,dq}}$ are the complex transfer function representations of the closed-loop gain and the closed-loop output admittance, respectively. The detailed expressions are shown as follows.

$$\mathbf{G_{cl,dq}} = \frac{\mathbf{T_{dq}}}{1+\mathbf{T_{dq}}} \qquad \mathbf{Y_{cl,dq}} = \frac{-\mathbf{Y_{LCLr}}}{1+\mathbf{T_{dq}}} \tag{12}$$

where $\mathbf{T_{dq}} = \mathbf{G_{c,dq}G_{del}Y_{LCLl}}$ is the complex transfer function representation of the open loop gain in dq-domain.

According to the relationship between complex transfer transfer function and transfer matrix shown in (1) and (2), $\mathbf{Y_{cl,dq}}$ can be represented in form of two-dimensional transfer matrix $Y_{cl,dq}^m$, shown as follows.

$$Y_{cl,dq}^m = \begin{bmatrix} \frac{\mathbf{Y_{LCLr}}(s-j\omega_1)}{1+G_{c,dq}G_{del}\mathbf{Y_{LCLl}}(s-j\omega_1)} & 0 \\ 0 & \frac{\mathbf{Y_{LCLr}}(s-j\omega_1)}{1+G_{c,dq}G_{del}\mathbf{Y_{LCLl}}(s-j\omega_1)} \end{bmatrix} \tag{13}$$

It can be seen from (13) that the d-axis and q-axis admittances are the same, and no coupling exists between them.

C. Effect of PLL on DQ Impedance Model

Due to the limited response speed of the PLL, the detected phase angle of the PCC voltage is not the same as the real phase angle when the steady-state PCC voltage is perturbed. To linearize the SRF-PLL in Fig. 1, a small perturbation is added to the PCC voltage, shown as

$$\begin{aligned}
&\mathbf{V_{PCC,dq}^c} = \mathbf{V_{PCC,dq}^s} \rightarrow \\
&\mathbf{V_{PCC,dq}^c} + \mathbf{\Delta V_{PCC,dq}^c} = e^{-j\Delta\theta_g}(\mathbf{V_{PCC,dq}^s} + \mathbf{\Delta V_{PCC,dq}^s})
\end{aligned} \tag{14}$$

where the superscripts **c** and **s** indicate that the symbols are represented in controller reference frame and system reference frame, respectively [7]. $\mathbf{V_{PCC,dq}^c}$ and $\mathbf{V_{PCC,dq}^s} = V_{PCC\_1d}$ are complex space vector representations of steady-state PCC

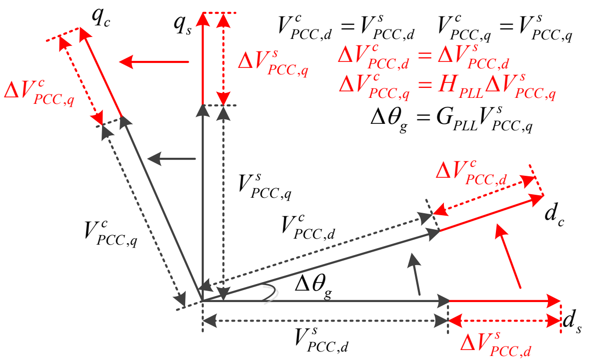

Fig. 3. Vector diagrams of PCC voltage in system and controller reference frames.

voltage in dq-domain in controller and system reference frames, respectively. In addition, $\mathbf{\Delta}$ denotes small-signal perturbation.

Since $e^{-j\Delta\theta_g}\approx 1-j\Delta\theta_g$ under small perturbation condition. The following small-signal relationship can be derived.

$$\begin{aligned}&\mathbf{\Delta V^c_{PCC,dq}}=\mathbf{\Delta V^s_{PCC,dq}}\underbrace{-j\Delta\theta_g V_{PCC\_1d}}_{\textbf{PLL}\quad\textbf{dynamics}}\rightarrow\\&\Delta V^c_{PCC,d}=\Delta V^s_{PCC,d}\\&\Delta V^c_{PCC,q}=\Delta V^s_{PCC,q}\underbrace{-\Delta\theta_g V_{PCC\_1d}}_{\textbf{PLL}\quad\textbf{dynamics}}\end{aligned}\tag{15}$$

It can be seen from (15) that the q-axis dynamic is influenced by PLL. By substituting $\Delta\theta_g=\Delta V^c_{PCC,q}tf_{PLL}/s$ into (15), (15) can be reformulated as follows.

$$\begin{aligned}&\Delta V^c_{PCC,d}=\Delta V^s_{PCC,d}\\&\Delta V^c_{PCC,q}=\frac{s}{\underbrace{s+tf_{PLL}V_{PCC\_1d}}_{\textbf{PLL}\quad\textbf{dynamics}}}\Delta V^s_{PCC,q}=H_{PLL}\Delta V^s_{PCC,q}\\&\Delta\theta_g=\frac{tf_{PLL}}{tf_{PLL}V_{PCC\_1d}+s}\Delta V^s_{PCC,q}=G_{PLL}\Delta V^s_{PCC,q}\end{aligned}\tag{16}$$

Based on (16), the vector diagrams of PCC voltage in system and controller reference frames under a small perturbation are shown in Fig. 3.

Similar with the linearization process of the abc/dq transformation of PLL in (14), the other abc/dq and dq/abc transformations in Fig. 2(a) can also be linearized, shown as follows.

$$\begin{aligned}&\mathbf{I^c_{g,dq}}=\mathbf{I^s_{g,dq}}\rightarrow\\&\mathbf{I^c_{g,dq}}+\mathbf{\Delta I^c_{g,dq}}=e^{-j\Delta\theta_g}(\mathbf{I^s_{g,dq}}+\mathbf{\Delta I^s_{g,dq}})\\&\mathbf{\Delta I^c_{g,dq}}=\mathbf{\Delta I^s_{g,dq}}\underbrace{-j\Delta\theta_g\mathbf{I^s_{g,dq}}}_{\textbf{PLL}\quad\textbf{dynamics}}\end{aligned}\tag{17}$$

$$\begin{aligned}&\mathbf{V^s_{c,dq}}=\mathbf{V^c_{c,dq}}\rightarrow\\&\mathbf{V^s_{c,dq}}+\mathbf{\Delta V^s_{c,dq}}=e^{j\Delta\theta_g}(\mathbf{V^c_{c,dq}}+\mathbf{\Delta V^c_{c,dq}})\\&\mathbf{\Delta V^s_{c,dq}}=\mathbf{\Delta V^c_{c,dq}}\underbrace{+j\Delta\theta_g\mathbf{V^c_{c,dq}}}_{\textbf{PLL}\quad\textbf{dynamics}}\end{aligned}\tag{18}$$

By substituting (16) into (17) and (18), the effects of PLL dynamics on abc/dq and dq/abc transformations can be derived as follows.

$$\begin{aligned}&\mathbf{\Delta I^{c,s}_{g,dq}}=\mathbf{\Delta I^c_{g,dq}}-\mathbf{\Delta I^s_{g,dq}}=-jG_{PLL}\Delta V^s_{PCC,q}\mathbf{I^s_{g,dq}}\\&\mathbf{\Delta V^{s,c}_{c,dq}}=\mathbf{\Delta V^s_{c,dq}}-\mathbf{\Delta V^c_{c,dq}}=jG_{PLL}\Delta V^s_{PCC,q}\mathbf{V^c_{c,dq}}\end{aligned}\tag{19}$$

To link $\mathbf{\Delta I^{c,s}_{g,dq}}$ and $\mathbf{\Delta V^{s,c}_{c,dq}}$ with $\mathbf{\Delta V^s_{PCC,dq}}$, $\Delta V^s_{PCC,q}$ should be represented as follows.

$$\Delta V^s_{PCC,q}=\frac{\mathbf{\Delta V^s_{PCC,dq}}-\mathbf{\Delta V^{s*}_{PCC,dq}}}{2j}\tag{20}$$

By substituting (20) into (19), (19) can be reformulated as follows.

$$\begin{aligned}&\mathbf{\Delta I^{c,s}_{g,dq}}=-\frac{G_{PLL}\mathbf{I^s_{g,dq}}}{2}(\mathbf{\Delta V^s_{PCC,dq}}-\mathbf{\Delta V^{s*}_{PCC,dq}})\\&\mathbf{\Delta V^{s,c}_{c,dq}}=\frac{G_{PLL}\mathbf{V^c_{c,dq}}}{2}(\mathbf{\Delta V^s_{PCC,dq}}-\mathbf{\Delta V^{s*}_{PCC,dq}})\end{aligned}\tag{21}$$

Based on (21), control block diagram of the GCI with consideration of PLL dynamics using complex space vectors and complex transfer functions can be established, as shown in Fig. 4. Similar with (11), the closed-loop system response $\mathbf{I_{g,dq}}$ can be derived as follows.

$$\mathbf{I^s_{g,dq}}=\mathbf{G^{PLL}_{cl,dq}}\mathbf{I^{ref}_{g,dq}}+\mathbf{Y^{PLL}_{cl,dq1}}\mathbf{V^s_{PCC,dq}}+\mathbf{Y^{PLL}_{cl,dq2}}\mathbf{V^{s*}_{PCC,dq}}\tag{22}$$

where $\mathbf{G^{PLL}_{cl,dq}}$ and $\mathbf{Y^{PLL}_{cl,dq}}$ are the complex transfer function representations of the closed-loop gain and the closed-loop output admittance with consideration of PLL dynamics, respectively. The detailed expressions are shown as follows.

$$\begin{aligned}&\mathbf{G^{PLL}_{cl,dq}}=\tfrac{\mathbf{T_{dq}}}{1+\mathbf{T_{dq}}}=\mathbf{G_{cl,dq}}\\&\mathbf{Y^{PLL}_{cl,dq1}}=\tfrac{-\mathbf{Y_{LCLr}}+(G_{PLL}\mathbf{V^c_{c,dq}}/2-G_{PLL}\mathbf{I^s_{g,dq}}\mathbf{G_{c,dq}}/2)\mathbf{G_{del}}\mathbf{Y_{LCLl}}}{1+\mathbf{T_{dq}}}\\&=\mathbf{Y_{cl,dq}}\underbrace{-(\frac{G_{PLL}\mathbf{I^s_{g,dq}}\mathbf{G_{cl,dq}}}{2}-\frac{G_{PLL}\mathbf{V^c_{c,dq}}\mathbf{G_{del}}\mathbf{Y_{LCLl}}}{2(1+\mathbf{T_{dq}})})}_{\textbf{PLL}\quad\textbf{dynamics}}\\&\mathbf{Y^{PLL}_{cl,dq2}}=\tfrac{-(G_{PLL}\mathbf{V^c_{c,dq}}/2-G_{PLL}\mathbf{I^s_{g,dq}}\mathbf{G_{c,dq}}/2)\mathbf{G_{del}}\mathbf{Y_{LCLl}}}{1+\mathbf{T_{dq}}}\\&=\underbrace{\frac{G_{PLL}\mathbf{I^s_{g,dq}}\mathbf{G_{cl,dq}}}{2}-\frac{G_{PLL}\mathbf{V^c_{c,dq}}\mathbf{G_{del}}\mathbf{Y_{LCLl}}}{2(1+\mathbf{T_{dq}})}}_{\textbf{PLL}\quad\textbf{dynamics}}\end{aligned}\tag{23}$$

It can be seen that $\mathbf{Y^{PLL}_{cl,dq1}}$ is affected by dynamics of both current control loop and PLL, whereas $\mathbf{Y^{PLL}_{cl,dq2}}$ is only affected by PLL dynamics. This finding paves the way of the proposed frequency scanning-based contributions identification method of current control loop and PLL on dq impedance characteristics.

According to (5), (22) can be reformulated as follows.

$$\begin{aligned}&\begin{bmatrix}\mathbf{I^s_{g,dq}}\\\mathbf{I^{s*}_{g,dq}}\end{bmatrix}=\begin{bmatrix}\mathbf{G^{PLL}_{cl,dq}}&\mathbf{0}\\\mathbf{0}&\mathbf{G^{PLL*}_{cl,dq}}\end{bmatrix}\begin{bmatrix}\mathbf{I^{ref}_{g,dq}}\\\mathbf{I^{ref*}_{g,dq}}\end{bmatrix}\cdots\\&+\begin{bmatrix}\mathbf{Y^{PLL}_{cl,dq1}}&\mathbf{Y^{PLL}_{cl,dq2}}\\\mathbf{Y^{PLL*}_{cl,dq2}}&\mathbf{Y^{PLL*}_{cl,dq1}}\end{bmatrix}\begin{bmatrix}\mathbf{V^s_{PCC,dq}}\\\mathbf{V^{s*}_{PCC,dq}}\end{bmatrix}\end{aligned}\tag{24}$$

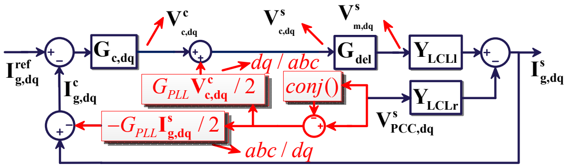

(a)

Fig. 4. Control block diagram of three-phase GCI in Fig. 1 using complex space vectors and complex transfer functions with considering PLL dynamics.

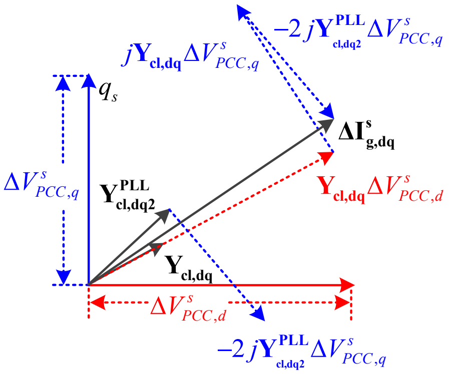

Fig. 5. Vector diagrams of $\Delta\mathbf{I}^{\mathbf{s}}_{\mathbf{g,dq,CC}}$ and $\Delta\mathbf{I}^{\mathbf{s}}_{\mathbf{g,dq,PLL}}$.

III. PROPOSED IMPEDANCE FEATURES DIVISION METHOD OF CURRENT CONTROL LOOP AND PLL

In this section, the derived complex transfer function-based dq impedance models in (13) and (24) are first compared. On its basis, the principle of the proposed frequency scanning-based identification method of contributions of current control loop and PLL on dq impedance model is explained.

A. Comparisons of Complex Transfer Functions-Based DQ Impedance Models (13) and (24)

It can be seen from (23) that

$$\mathbf{Y}^{\mathbf{PLL}}_{\mathbf{cl,dq1}} = \mathbf{Y}_{\mathbf{cl,dq}} - \mathbf{Y}^{\mathbf{PLL}}_{\mathbf{cl,dq2}} \tag{25}$$

It can be seen from (22) that when a small perturbation $\Delta\mathbf{V}^{\mathbf{s}}_{\mathbf{PCC,dq}} = \Delta V^s_{PCC,d} + j\Delta V^s_{PCC,q}$ is added to steady-state $\mathbf{V}^{\mathbf{s}}_{\mathbf{PCC,dq}}$, small-signal response of $\mathbf{I}^{\mathbf{s}}_{\mathbf{g,dq}}$ when $\mathbf{I}^{\mathbf{ref}}_{\mathbf{g,dq}} = 0$ can be derived as follows.

$$\begin{aligned}\Delta\mathbf{I}^{\mathbf{s}}_{\mathbf{g,dq}}\big|_{\mathbf{I}^{\mathbf{ref}}_{\mathbf{g,dq}}=0} &= (\mathbf{Y}_{\mathbf{cl,dq}} - \mathbf{Y}^{\mathbf{PLL}}_{\mathbf{cl,dq2}})(\Delta V^s_{PCC,d} \quad \cdots \\ &\quad + j\Delta V^s_{PCC,q}) + \mathbf{Y}^{\mathbf{PLL}}_{\mathbf{cl,dq2}}(\Delta V^s_{PCC,d} - j\Delta V^s_{PCC,q}) \\ &= \mathbf{Y}_{\mathbf{cl,dq}}(\Delta V^s_{PCC,d} + j\Delta V^s_{PCC,q}) - 2j\mathbf{Y}^{\mathbf{PLL}}_{\mathbf{cl,dq2}}\Delta V^s_{PCC,q} \\ &= \Delta\mathbf{I}^{\mathbf{s}}_{\mathbf{g,dq,CC}} + \Delta\mathbf{I}^{\mathbf{s}}_{\mathbf{g,dq,PLL}}\end{aligned} \tag{26}$$

where $\Delta\mathbf{I}^{\mathbf{s}}_{\mathbf{g,dq,CC}}$ and $\Delta\mathbf{I}^{\mathbf{s}}_{\mathbf{g,dq,PLL}}$ are the small-signal responses related with current control loop and PLL, respectively. It can be seen that if $\Delta V^s_{PCC,q} = 0$, the small-signal response is only related with current control loop. Fig. 5 shows the vector diagrams of $\Delta\mathbf{V}^{\mathbf{s}}_{\mathbf{PCC,dq}}$ and $\Delta\mathbf{I}^{\mathbf{s}}_{\mathbf{g,dq}}$.

On the other hand, (24) can be represented by transfer matrices, shown as follows.

$$I^s_{g,dq} = G^{PLL,m}_{cl,dq} I^{ref}_{g,dq} + Y^{PLL,m}_{cl,dq} V^s_{PCC,dq} \tag{27}$$

where $Y^{PLL,m}_{cl,dq}$ can be derived as [27]

$$\begin{aligned}Y^{PLL,m}_{cl,dq} &= \begin{bmatrix} Y^{PLL}_{cl,dd} & Y^{PLL}_{cl,dq} \\ Y^{PLL}_{cl,qd} & Y^{PLL}_{cl,qq}\end{bmatrix} \\ &= (A^m_Z)^{-1}\begin{bmatrix}\mathbf{Y}^{\mathbf{PLL}}_{\mathbf{cl,dq1}} & \mathbf{Y}^{\mathbf{PLL}}_{\mathbf{cl,dq2}} \\ \mathbf{Y}^{\mathbf{PLL*}}_{\mathbf{cl,dq2}} & \mathbf{Y}^{\mathbf{PLL*}}_{\mathbf{cl,dq1}}\end{bmatrix} A^m_Z\end{aligned} \tag{28}$$

where $A^m_Z = \frac{1}{\sqrt{2}}\begin{bmatrix}1 & j \\ 1 & -j\end{bmatrix}$. By substituting (25) into (28), the four elements of the $Y^{PLL,m}_{cl,dq}$ are calculated as follows.

$$\begin{aligned}Y^{PLL}_{cl,dd} &= \frac{\mathbf{Y}_{\mathbf{cl,dq}} + \mathbf{Y}^{*}_{\mathbf{cl,dq}}}{2} \\ Y^{PLL}_{cl,dq} &= j\Big(\frac{\mathbf{Y}_{\mathbf{cl,dq}} - \mathbf{Y}^{*}_{\mathbf{cl,dq}}}{2} \underbrace{-\mathbf{Y}^{\mathbf{PLL}}_{\mathbf{cl,dq2}} + \mathbf{Y}^{\mathbf{PLL*}}_{\mathbf{cl,dq2}})}_{\mathbf{PLL\ \ dynamics}} \\ Y^{PLL}_{cl,qd} &= j\frac{\mathbf{Y}^{*}_{\mathbf{cl,dq}} - \mathbf{Y}_{\mathbf{cl,dq}}}{2} \\ Y^{PLL}_{cl,qq} &= \frac{\mathbf{Y}_{\mathbf{cl,dq}} + \mathbf{Y}^{*}_{\mathbf{cl,dq}}}{2} \underbrace{-(\mathbf{Y}^{\mathbf{PLL}}_{\mathbf{cl,dq2}} + \mathbf{Y}^{\mathbf{PLL*}}_{\mathbf{cl,dq2}})}_{\mathbf{PLL\ \ dynamics}}\end{aligned} \tag{29}$$

It can be seen from (29) that $Y^{PLL}_{cl,dq}$ and $Y^{PLL}_{cl,qq}$ are affected by PLL dynamics.

B. Proposed Impedance Features Division Method of Current Control Loop and PLL

By adding a small-signal perturbation $\Delta V^s_{PCC,dq1}$ to $V^s_{PCC,dq}$ when $I^{ref}_{g,dq} = [0,0]^T$, the small-signal response of $I^s_{g,dq}$ is shown as follows.

$$\begin{bmatrix}\Delta I^s_{g,d1} \\ \Delta I^s_{g,q1}\end{bmatrix}\Bigg|_{I^{ref}_{g,dq}=[0,0]^T} = \begin{bmatrix} Y^{PLL}_{cl,dd} & Y^{PLL}_{cl,dq} \\ Y^{PLL}_{cl,qd} & Y^{PLL}_{cl,qq}\end{bmatrix}\begin{bmatrix}\Delta V^s_{PCC,d1} \\ \Delta V^s_{PCC,q1}\end{bmatrix} \tag{30}$$

By substituting (29) into (30) and setting $\Delta V^s_{PCC,q1} = 0$, (30) can be reformulated as

$$\begin{aligned}\Delta I^s_{g,d1} &= \frac{\mathbf{Y}_{\mathbf{cl,dq}} + \mathbf{Y}^{*}_{\mathbf{cl,dq}}}{2}\Delta V^s_{PCC,d1} \\ \Delta I^s_{g,q1} &= j\frac{\mathbf{Y}^{*}_{\mathbf{cl,dq}} - \mathbf{Y}_{\mathbf{cl,dq}}}{2}\Delta V^s_{PCC,d1}\end{aligned} \tag{31}$$

The impedance characteristics of the current control loop can be obtained from (31), shown as

$$\begin{aligned}\frac{\mathbf{Y}_{\mathbf{cl,dq}} + \mathbf{Y}^{*}_{\mathbf{cl,dq}}}{2} &= \frac{\Delta I^s_{g,d1}}{\Delta V^s_{PCC,d1}} \\ \frac{\mathbf{Y}_{\mathbf{cl,dq}} - \mathbf{Y}^{*}_{\mathbf{cl,dq}}}{2} &= j\frac{\Delta I^s_{g,q1}}{\Delta V^s_{PCC,d1}}\end{aligned} \tag{32}$$

In addition, by adding a small-signal perturbation $\Delta V^s_{PCC,dq2} = [0, V^s_{PCC,q2}]^T$ to $V^s_{PCC,dq}$ when $I^{ref}_{g,dq} = [0,0]^T$, the small-signal response of $I^s_{g,dq}$ is shown as follows.

$$\begin{aligned}\Delta I^s_{g,d2} &= -\Big(\frac{\Delta I^s_{g,q1}}{\Delta V^s_{PCC,d1}} + j(\mathbf{Y}^{\mathbf{PLL}}_{\mathbf{cl,dq2}} - \mathbf{Y}^{\mathbf{PLL*}}_{\mathbf{cl,dq2}})\Big)\Delta V^s_{PCC,q2} \\ \Delta I^s_{g,q2} &= \Big(\frac{\Delta I^s_{g,d1}}{\Delta V^s_{PCC,d1}} - (\mathbf{Y}^{\mathbf{PLL}}_{\mathbf{cl,dq2}} + \mathbf{Y}^{\mathbf{PLL*}}_{\mathbf{cl,dq2}})\Big)\Delta V^s_{PCC,q2}\end{aligned} \tag{33}$$

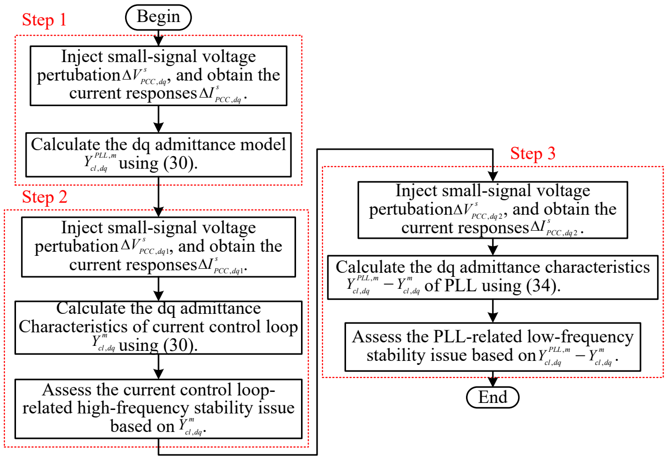

Fig. 6. Flowchart of the proposed frequency scanning-based contributions identification method of current control loop and PLL on dq impedance characteristics.

The impedance characteristics of the PLL can be obtained from (33), shown as

$$\begin{aligned} \mathbf{Y^{PLL}_{cl,dq2}} - \mathbf{Y^{PLL*}_{cl,dq2}} &= j\Big(\frac{\Delta I^{s}_{g,q1}}{\Delta V^{s}_{PCC,d1}} + \frac{\Delta I^{s}_{g,d2}}{\Delta V^{s}_{PCC,q2}}\Big) \\ \mathbf{Y^{PLL}_{cl,dq2}} + \mathbf{Y^{PLL*}_{cl,dq2}} &= \frac{\Delta I^{s}_{g,d1}}{\Delta V^{s}_{PCC,d1}} - \frac{\Delta I^{s}_{g,q2}}{\Delta V^{s}_{PCC,q2}} \end{aligned} \tag{34}$$

Note that if small-signal current perturbation is injected into the GCI system in parallel way, the PCC voltage responses will be affected by dynamics of both current control loop and PLL no matter what $\Delta V^{s}_{PCC,d}$ and $\Delta V^{s}_{PCC,q}$ are, i.e., the impedance characteristics of the two control loops cannot be partitioned.

The flowchart of the proposed frequency scanning-based contributions identification method of current control loop and PLL on dq impedance model is shown in Fig. 6. In step 1, small-signal voltage perturbation $\Delta V^{s}_{PCC,dq}$ is injected into PCC in series way, and grid current responses $\Delta I^{s}_{PCC,dq}$ is obtained. On its basis, the dq admittance model is calculated using (30). In step 2, small-signal voltage perturbation $\Delta V^{s}_{PCC,dq} = [\Delta V^{s}_{PCC,d1}, 0]$ in injected into PCC in series way, and grid current responses $\Delta I^{s}_{PCC,dq1}$ is obtained, based on which the impedance characteristic of current control loop $Y^{m}_{cl,dq}$ is calculated using (32). The calculated $Y^{m}_{cl,dq}$ can then be used to assess the high-frequency stability issue. In step 3, small-signal voltage perturbation $\Delta V^{s}_{PCC,dq} = [0, \Delta V^{s}_{PCC,q2}]$ in injected into PCC in series way, and grid current responses $\Delta I^{s}_{PCC,dq2}$ is obtained, based on which the impedance characteristic of PLL is calculated using (34). The calculated dq impedance characteristics of PLL can then be used to assess the low-frequency stability issue.

IV. SIMULATION VERIFICATION

In this section, the effectiveness of the proposed dq-domain impedance characteristics division method is verified by the frequency scanning results and time-domain simulation results in Matlab/Simulink.

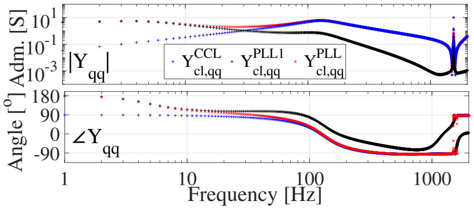

Fig. 7. Measured Bode diagrams of the q-axis admittance components in step 1, step 2 and step 3 of Fig. 6.

The circuit and controller parameters of the GCI in Fig. 1 are shown in Table I. Since the q-axis impedance component of the dq impedance model plays an important role in stability assessment, the following frequency scanning results will focus on the q-axis impedance characteristics.

TABLE I
CIRCUIT AND CONTROLLER PARAMETERS OF THE GCI

Parameter	Value
DC-link voltage V_{dc}	1150 V
Grid fundamental frequency f_1	50 Hz
Inverter side filter inductance L_{f1}	263 μH
Grid side filter inductance L_{f2}	200 μH
Filter capacitance C_f	40 μF
Switching frequency f_{swit}	2.5 kHz
Sampling frequency f_{samp}	2.5 kHz
Grid Vrms (phase-to-phase) V_g	575 V
Proportional gain of current controller k_{pi}	5.4908e-04
Integral gain of current controller k_{ii}	0.3295
Proportional gain of PLL k_{ppll}	40
Integral gain of PLL k_{ipll}	800
D-axis current reference $I^{ref}_{g,d}$	2.0 kA
Integral gain of PLL $I^{ref}_{g,q}$	0

The measured Bode diagrams of the q-axis admittance component in step 1, step 2 and step 3 of Fig. 6 are shown as $Y^{PLL}_{cl,qq}$, $Y^{CCL}_{cl,qq}$ and $Y^{PLL1}_{cl,qq}$ in Fig. 7, respectively. It can be seen that the high-frequency admittance characteristic and low-frequency admittance characteristic can be extracted in step 2 and step 3, respectively, which verifies the effectiveness of the proposed impedance features division method in Section III-B.

Next, the extracted high-frequency admittance characteristic $Y^{CCL}_{cl,qq}$ is used to assess the stability issue related with current control loop. Fig. 8(a) shows the Bode diagrams of $Y^{CCL}_{cl,qq}$ and q-axis admittance component of a 2 km transmission line $Y^{TL2}_{cl,qq}$. It can be seen that the phase angle difference at the magnitude interaction point 799 Hz is $86.92^{o} - (-95.43^{o}) = 182.35^{o}$, which indicates that the system is unstable at 799 Hz. Fig. 8(b) shows the time-domain simulation results of three-phase grid currents, and the FFT is shown in Fig. 8(c). It can be seen that the three-phase grid currents oscillate at 780 Hz, which agree with the theoretical analysis results in Fig. 8(a).

Next, the extracted low-frequency admittance characteristic $Y^{PLL1}_{cl,qq}$ is used to assess the stability issue related with PLL. Fig. 9(a) shows the Bode diagrams of $Y^{PLL1}_{cl,qq}$ and q-axis admittance component of a 21 km transmission line $Y^{TL1}_{cl,qq}$. It can be seen that the phase angle difference at the magnitude

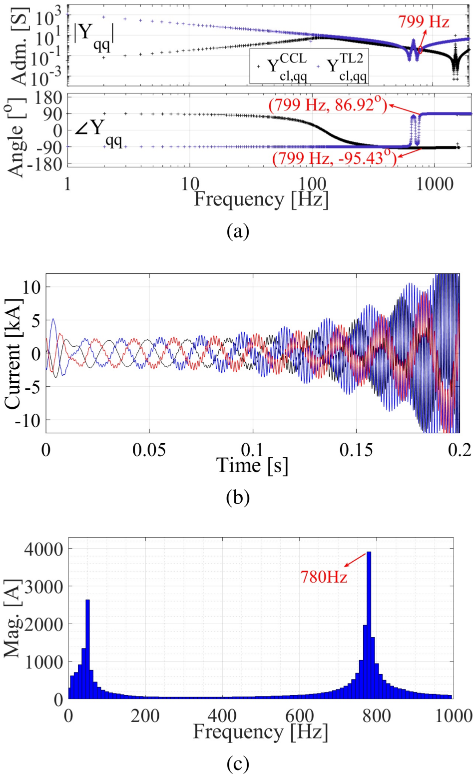

Fig. 8. High-frequency stability analysis based on the extracted admittance characteristics of current control loop. (a) Bode diagrams of $Y_{cl,qq}^{CCL}$ and $Y_{cl,qq}^{TL2}$. (b) Time-domain simulation results of grid currents. (c) FFT of grid currents.

interaction point 14 Hz is $110.1^{o} - (-82.5^{o}) = 192.6^{o}$, which indicates that the system is unstable at 14 Hz. Fig. 9(b) shows the time-domain simulation results of three-phase grid currents, and the FFT is shown in Fig. 9(c). It can be seen that the three-phase grid currents mainly oscillate at 66 Hz (50+16=66 Hz), which agree with the theoretical analysis results in Fig. 9(a).

V. CONCLUSION

This paper presents a frequency scanning-based black box identification method of the contributions of current control loop and PLL on dq-domain impedance characteristics of the GCI without knowing internal circuit and controller parameters. Small-signal three-phase voltage perturbation is injected to excite the grid current responses for extracting the dq-domain impedance characteristics of current control loop and PLL. The theoretical analysis results, frequency scanning results and time-domain simulation results obtained in Matlab/Simulink environment verify the effectiveness of the presented dq-domain impedance characteristics division method. The frequency scanning-based contributions identification of other control loops, e.g., outer power control loop and dc-link voltage control, will be investigated in a future work.

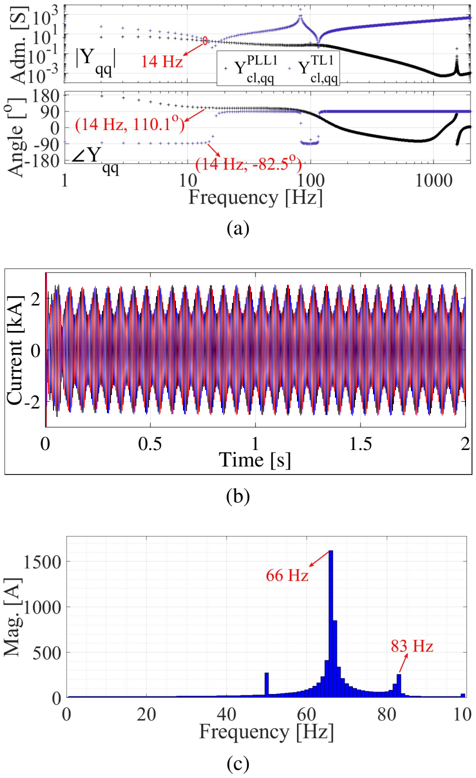

Fig. 9. Low-frequency stability analysis based on the extracted admittance characteristics of PLL. (a) Bode diagrams of $Y_{cl,qq}^{PLL1}$ and $Y_{cl,qq}^{TL1}$. (b) Time-domain simulation results of grid currents. (c) FFT of grid currents.

ACKNOWLEDGMENT

The authors wish to thank Mrs. Pengli Yang from Institute of Microelectronics, Chinese Academy of Sciences for her valuable discussions and suggestions.

REFERENCES

[1] F. Blaabjerg, Z. Chen, and S. B. Kjaer, “Power electronics as efficient interface in dispersed power generation systems,” *IEEE Trans. Power Electron.*, vol. 19, no. 5, pp. 1184–1194, Sep. 2004.

[2] X. Wang and F. Blaabjerg, “Harmonic stability in power electronic-based power systems: Concept, modeling, and analysis,” *IEEE Trans. Smart Grid*, vol. 10, no. 3, pp. 2858–2870, May 2019.

[3] W. Zhou, Y. Wang, and Z. Chen, “Impedance-decoupled modelling method of multi-port transmission network in inverter-fed power plant,” *IEEE Trans. Ind. Appl.*, vol. 56, no. 1, pp. 611–621, Jan.-Feb. 2020.

[4] W. Zhou, Y. Wang, D. Liu, and Z. Chen, “Optimization of active and reactive power dispatch among multi-paralleled grid-connected inverters considering low-frequency stability,” in *Proc. IEEE 2019 45th Annual Conference of the IEEE Industrial Electronics Society (IES)*, pp. 6158–6165.

[5] D. Dong, B. Wen, D. Boroyevich, P. Mattavelli, and Y. Xue, “Analysis of phase-locked loop low-frequency stability in three-phase grid-connected power converters considering impedance interactions,” *IEEE Trans. Ind. Electron.*, vol. 62, no. 1, pp. 310–321, Jan. 2015.

[6] J. Sun, “Impedance-based stability criterion for grid-connected inverters,” *IEEE Trans. Power Electron.*, vol. 26, no. 11, pp. 3075–3078, Nov. 2011.

[7] B. Wen, D. Boroyevich, R. Burgos, P. Mattavelli, and Z. Shen, “Analysis of DQ small-signal impedance of grid-tied inverters,” *IEEE Trans. Power Electron.*, vol. 31, no. 1, pp. 675–687, Jan. 2016.

[8] W. Zhou, Y. Wang, R. E. Torres-Olguin, D. Liu, and Z. Chen, "A modified dq impedance model of three-phase grid-connected inverter-grid system considering coupling between inverter and grid," in *Proc. IEEE 2020 35th Applied Power Electronics Conference and Exposition (APEC)*, pp. 1–8.

[9] W. Zhou, Y. Wang, and Z. Chen, "A gray-box parameters identification method of voltage source converter using vector fitting algorithm," in *Proc. IEEE 2019 10th International Conference on Power Electronics and ECCE Asia (ICPE 2019-ECCE Asia)*, pp. 2948–2955.

[10] W. Zhou, Y. Wang, P. Cai, and Z. Chen, "A gray-box impedance reshaping method of grid-connected inverter for resonance damping," in *Proc. IEEE 2019 10th International Conference on Power Electronics and ECCE Asia (ICPE 2019-ECCE Asia)*, pp. 2660–2667.

[11] J. Huang, K. A. Corzine, and M. Belkhayat, "Small-signal impedance measurement of power-electronics-based AC power systems using line-to-line current injection," *IEEE Trans. Power Electron.*, vol. 24, no. 2, pp. 445–455, Feb. 2009.

[12] G. Francis, R. Burgos, D. Boroyevich, F. Wang, and K. Karimi, "An algorithm and implementation system for measuring impedance in the DQ domain," in *Proc. IEEE 2011 IEEE Energy Conversion Congress and Exposition*, pp. 3221–3228.

[13] V. Valdivia, A. Lázaro, A. Barrado, P. Zumel, C. Fernández, and M. Sanz, "Impedance identification procedure of three-phase balanced voltage source inverters based on transient response measurements," *IEEE Trans. Power Electron.*, vol. 26, no. 12, pp. 3810–3816, Dec. 2011.

[14] Z. Shen, M. Jaksic, P. Mattavelli, D. Boroyevich, J. Verhulst, and M. Belkhayat, "Design and implementation of three-phase AC impedance measurement unit (IMU) with series and shunt injection," in *Proc. IEEE 2013 Twenty-Eighth Annual IEEE Applied Power Electronics Conference and Exposition (APEC)*, pp. 2674–2681.

[15] A. Rygg and M. Molinas, "Apparent impedance analysis: A small-signal method for stability analysis of power electronic-based systems," *IEEE J. Emerg. Sel. Top. Power Electron.*, vol. 5, no. 4, pp. 1474–1486, Dec. 2017.

[16] M. Jaksic, D. Boroyevich, R. Burgos, Z. Shen, I. Cvetkovic, and P. Mattavelli, "Modular interleaved single-phase series voltage injection converter used in small-signal dq impedance identification," in *Proc. IEEE 2014 Energy Conversion Congress and Exposition (ECCE)*, pp. 3036–3045.

[17] Y. Tang, R. Burgos, B. Wen, D. Boroyevich, J. Verhulst, D. Vrtachnik, and M. Belkhayat, "A novel DQ impedance measurement method in three-phase balanced systems," in *Proc. IEEE 2019 20th Workshop on Control and Modeling for Power Electronics (COMPEL)*, pp. 1–5.

[18] Y. Zhang, X. Du, Y. Shi, C. Zeng, J. Liu, and H.-M. Tai, "Impedance scanning method of grid-tied converters under nonzero grid impedance condition," in *Proc. IEEE 2019 10th International Symposium on Power Electronics for Distributed Generation Systems (PEDG)*, pp. 728–733.

[19] W. Cao, Y. Ma, X. Zhang, and F. Wang, "Sequence impedance measurement of three-phase inverters using a parallel structure," in *Proc. IEEE 2015 Applied Power Electronics Conference and Exposition (APEC)*, pp. 3031–3038.

[20] X. Yue, Z. Fang, F. Wang, Z. Zhang, and H. Shi, "A novel adaptive frequency injection method for power electronic system impedance measurement," *IEEE Trans. Power Electron.*, vol. 29, no. 12, pp. 6700–6711, Dec. 2014.

[21] T. Roinila, T. Messo, and E. Santi, "MIMO-identification techniques for rapid impedance-based stability assessment of three-phase systems in DQ domain," *IEEE Trans. Power Electron.*, vol. 33, no. 5, pp. 4015–4022, May 2018.

[22] A. Riccobono, M. Mirz, and A. Monti, "Noninvasive online parametric identification of three-phase AC power impedances to assess the stability of grid-tied power electronic inverters in LV networks," *IEEE J. Emerg. Sel. Top. Power Electron.*, vol. 6, no. 2, pp. 629–647, Jun. 2018.

[23] T. Roinila, H. Abdollahi, S. Arrua, and E. Santi, "Real-time stability analysis and control of multiconverter systems by using MIMO-identification techniques," *IEEE Trans. Power Electron.*, vol. 34, no. 4, pp. 3948–3957, Apr. 2019.

[24] L. Harnefors, "Modeling of three-phase dynamic systems using complex transfer functions and transfer matrices," *IEEE Trans. Ind. Electron.*, vol. 54, no. 4, pp. 2239–2248, Aug. 2007.

[25] X. Wang, L. Harnefors, and F. Blaabjerg, "Unified impedance model of grid-connected voltage-source converters," *IEEE Trans. Power Electron.*, vol. 33, no. 2, pp. 1775–1787, Feb. 2018.

[26] W. Zhou, Y. Wang, R. E. Torres-Olguin, and Z. Chen, "Effect of reactive power characteristic of offshore wind power plant on low-frequency stability," *IEEE Trans. Energy Convers.*, vol. 35, no. 2, pp. 837–853, Jun. 2020.

[27] A. Rygg, M. Molinas, C. Zhang, and X. Cai, "On the equivalence and impact on stability of impedance modeling of power electronic converters in different domains," *IEEE J. Emerg. Sel. Top. Power Electron.*, vol. 5, no. 4, pp. 1444–1454, Dec. 2017.